Environmental Science and Pollution Research (2019) 26:22082–22096
https://doi.org/10.1007/s11356-019-05570-8

RESEARCH ARTICLE

Preparation of AgCl/TNTs nanocomposites for organic dyes and inorganic heavy metal removal

Cheng-Yen Tsai[1] · Chen-Wuing Liu[1] · Hsing-Cheng Hsi[2] · Kuen-Song Lin[3] · Yi-Wen Lin[1] · Li-Chi Lai[1] · Tsung-Nan Weng[1]

Received: 18 January 2019 / Accepted: 24 May 2019 / Published online: 30 May 2019

Abstract

In this study, TiO_2 nanotubes (TNTs) and AgCl-modified TNTs nanocomposites with multiple crystal phases were synthesized through a hydrothermal method without calcination. The resultant samples had a large Brunauer-Emmett-Teller surface area. Additionally, the Ag modification process reduced the recombination rate of electron-hole pairs in the synthesized sample and possessed more oxygen vacancy sites. The surface area of the AgCl-modified TNTs was smaller than that of non-modified TNTs sample; however, the nanocomposites exhibited outstanding photocatalytic performance and adsorption properties. AgCl compounds present on the TNTs surface effectively interacted with Hg^0, improving the dye photodegradation efficiency. The Hg^0 removal efficiencies of the TNTs and AgCl-modified TNTs samples were about 63% and 86%, respectively. The crystal violet (CV) and malachite green (MG) removal efficiencies of the AgCl-modified TNTs sample were around 57% and 72%, respectively. Both dyes photodecomposition efficiencies for AgCl-modified TNTs sample are higher than those of TNTs sample. The oxygen vacancy on the AgCl-modified TNTs surface was determined to be advantageous for OH^- and arsenate adsorption through ligand exchange. The maximum adsorption quantity of As^{5+} calculated by Langmuir equation was 15.38 mg g^{-1} (TNTs) and 21.10 mg g^{-1} (AgCl-modified TNTs).

Keywords Hydrothermal method · Photocatalysts · Elemental mercury · Arsenate · Dye

Introduction

Gaseous and aqueous environments contain various pollutants such as organic contaminants or inorganic heavy metals. Gas-phase mercury (Hg) emission from anthropogenic sources is a global concern. Coal-fired power plants constitute the primary source of Hg emissions (Pacyna et al. 2010). The major Hg species in exhausts are elemental (Hg^0), oxidized (Hg^{2+}), and particle-bond (Hg_p) (Hsi et al. 2010). Among these species, Hg^{2+} and Hg_p can be easily removed using traditional air pollution control devices or technologies (e.g., wet flue gas desulfurization). By contrast, removing Hg^0 using traditional air pollution control devices is difficult because it is highly volatile and insoluble in water. In addition, organic dyes and heavy metals in aqueous phase have significant harmful effects on aquatic animals and human beings. Various organic dyes such as crystal violet, malachite green, Congo red, and safranin-O are used in dyeing clothes and in handlooms. The discharged dye wastewater may pollute surface water and groundwater. Abukhadra et al. (2018) fabricated bentonite/polyaniline@Ni_2O_3 composite for removing safarnin-O dye, which can be completely removed after 90 min. Mohamed et al. (2018) synthesized polypyrrole nanofiber/Zn-Fe layered double hydroxide nanocomposites for the safranin dye removal, and synthetic nanocomposite can be used for six cycles. Apart from organic pollutants, groundwater ammonia and heavy metals, such as arsenate (As^{5+}) and hexavalent chromium (Cr^{6+}), are also relatively common contaminants. Shaban

Responsible editor: Suresh Pillai

✉ Chen-Wuing Liu
cwliu@ntu.edu.tw

[1] Department of Bioenvironmental Systems Engineering, National Taiwan University, No. 1, Section 4, Roosevelt Road, Taipei 106, Taiwan

[2] Graduate Institute of Environmental Engineering, National Taiwan University, No. 71, Chou-Shan Road, Taipei 106, Taiwan

[3] Department of Chemical Engineering and Materials Science, Yuan Ze University, No. 135, Yuan-Tung Road, Chung-Li, Taoyuan City 320, Taiwan

et al. (2017) prepared zeolite Na-A which had a high efficiency in the removal of ammonia and other water pollutants. Shaban et al. (2018) synthesized graphene oxide and polyaniline for removing Cr^{6+} contaminants from aqueous solutions. Recently, Abukhadra et al. (2019) investigated Cr^{6+} and Congo red dye removal by using bentonite/chitosan@cobalt oxide composite (BE/CH@Co). The adsorption capacity of BE/CH@Co was 303 mg g^{-1} for Congo red and 250 mg g^{-1} for Cr^{6+}. Adsorptive techniques are usually applied to remove the aforementioned contaminants; such techniques are commonly applied because of their operational simplicity and cost-effectiveness. However, in recent years, titanium dioxide (TiO_2) photocatalyst nanoparticles have been frequently studied for their ability to adsorb and decompose contaminants.

An ideal absorbent should have a high surface area, uniformly accessible pores, and physical/chemical stability. TiO_2 nanotubes (TNTs) are considered highly efficient oxidizers and adsorbents for removing organic pollutants and heavy metals in gaseous and aqueous phases because of their large specific surface areas and various functional hydroxyl groups. Moreover, transition metal cations and alkali can be exchanged with protons of OH groups in aqueous solutions (Bavykin et al. 2005, 2006).

Improving the TiO_2 electron-hole (e^-/h^+) separation time is one of the methods to enhance photocatalytic activity. Metal modification of the TiO_2 surface is an effective method for increasing the separation time of photogenerated electrons and holes. Several metals, such as Ag, Fe, and Pd, have been used to modify the surface of TiO_2, resulting in excellent photocatalytic activity (Yu et al. 2009; Li et al. 2017; Narayani et al. 2018). Ag has low toxicity, adequate bactericidal capability, and low cost; thus, it is commonly used as a modified precursor. Synthesizing Ag nanoparticles on the surface of AgX (X = Br, I, or Cl) can increase the stability of AgX and can induce photogenerated electrons to shift preferentially to Ag nanoparticles rather than the Ag^+ ions in AgX (Wang et al. 2008; Tian and Zhang 2012; Tian et al. 2014). Wang et al. (2008) synthesized a Ag@AgCl photocatalyst by using Ag_2MoO_4 with HCl to fabricate AgCl particles and then reduce Ag^+ ions in the AgCl particles to Ag^0 species. In addition, applying a hydrothermal process for synthesizing TNTs requires the use of HCl acid washing. Therefore, after hydrothermal synthesis, applying HCl to oxidize Ag can lead to the formation of AgCl; this may be a feasible method for fabricating highly efficient AgCl/TNTs photocatalysts. Nevertheless, no study has been conducted on this method.

We previously developed a simple synthesis process for fabricating TNTs nanocomposites. The TNTs nanocomposites were fabricated without calcination, engendering large specific surface areas (Tsai et al. 2017). In the current study, we employed the aforementioned synthesis process by using Ag_2O and Degussa P-25 as precursors to manufacture AgCl-modified TNTs nanocomposites. Moreover, we studied the formed samples for determining organic dye photodegradation and heavy metal removal; the dyes were crystal violet (CV) and malachite green (MG), and the metals were aqueous-solution As^{5+} and gas-phase Hg^0. We also examined the removal mechanisms. Notably, approaches for producing Ag-modified TNTs nanocomposites for dye and heavy metal removal are few, particularly those for removing As^{5+} and Hg^0.

Experimental

TNTs and AgTs fabrication

Commercial TiO_2 nanoparticles (Degussa P-25 TiO_2) and Ag_2O (Alfa Aesar) were used as precursors for fabricating non-modified TNTs and AgCl-modified TNTs (AgTs) composites by using an alkaline hydrothermal method. The hydrothermal process resemble to those in the literature (Kasuga et al. 1999; Tsai et al. 2017). TNTs were synthesized by mixing 200 mL of 10 M NaOH aqueous solution and 5 g of Degussa P-25 TiO_2 nanopowder, pacing the mixture in an autoclave, and heating at 130 °C for 24 h. The as-prepared samples were then washed alternatively with distilled water and 0.5 N HCl solution for several times. Subsequently, the samples were dried at 100 °C for 24 h. AgTs were synthesized through a similar process, with 10 wt% Ag_2O powder being added.

As-prepared samples characterizations

A powder X-ray diffraction (XRD) instrument (Bruker, D2 Phaser) with Cu Kα radiation ($\lambda = 1.5405$ Å) was utilized to examine the crystal phase of the as-prepared samples. The JCPDS database was applied to identify the crystalline phases of the samples. The total surface area (S_{BET}), total pore volume (V_{total}), and pore size distribution of the as-prepared samples were analyzed on the basis of the N_2 adsorption outcome acquired at 77 K (Micromeritics ASAP 2020). S_{BET} was calculated using the Brunauer-Emmett-Teller (BET) equation based on the ASTM D4820-96a method. The Barrett-Joyner-Halenda (BJH) method was employed for establishing the mesopore size distribution (Gregg and Sing 1982). The morphology of the resultant products was determined using a transmission electron microscope (TEM; Hitachi H-7100) and high-resolution transmission electron microscope (HR-TEM; Philips/Tecnai F30) through visual counting. Furthermore, a field-emission scanning electron microscope (FE-SEM; Hitachi SU8220) coupled with an energy-dispersive spectrometer (EDS) was used to examine the resultant samples. The diffuse reflectance UV-visible (UV-vis) spectra of the samples were observed in the range of 250–

800 nm by employing a spectrophotometer (JASCO V-650). Photoluminescence (PL) spectroscopy was performed using a fluorescence spectrometer (Horiba Fluoro Max-4). An X-ray photoelectron spectroscope (XPS; VG Scientific ESCALAB 250) was also used to determine the compositions and Ti, O, and Ag bonding patterns. The obtained XPS spectra were deconvoluted using XPSPEAK® software.

Gas-phase Hg^0 photocatalytic experiments

The resultant TNTs and AgTs samples were evaluated for determining their efficiency in removing gas-phase Hg^0. The experimental equipment and method were similar to those used in our previous studies (Hsi and Tsai 2012; Chen et al. 2014). The experimental apparatus comprised a mixed gas generation unit, photochemical quartz reactor, and gas-phase Hg^0 analysis system. The total gas flow rate was 0.2 L min^{-1}, with a Hg^0 concentration of 250 μg Nm^{-3}. A sample of 10 mg was placed on two pieces of glass and was set in the quartz reactor. A UV lamp (80 W, Raceahead Co., Taiwan) with a light intensity of 8.0 ± 0.5 mW/cm^2 (Sentry UVC-ST512), which exhibited a major sharp peak at 254 nm (Rainbow Light RLS-1000, Taiwan), was placed at a distance of approximately 13 cm from the quartz reactor. Gas-phase Hg^0 removal experiments were performed at atmospheric pressure and room temperature. The Hg^0 concentration was determined using a gold amalgamation system (Brooks Rand model AC-01) and a cold-vapor atomic fluorescence spectrophotometer (Brooks Rand Lab model III). Each complete run required 6 min, and 50 runs were carried out for each synthesized sample.

Aqueous solution organic dye and arsenate removal tests

The photocatalytic activity of the as-prepared products was evaluated on the basis of the photodegradation of CV (Sigma-Aldrich) and MG (Sigma-Aldrich) dyes. Moreover, oxidizing radical trapping experiments are also carried out in this study, which added 10 ppm L-ascorbic acid (Scharlau). Ten milligrams of the prepared sample and 15 ppm of aqueous dye solution were mixed in a 100-mL photochemical reactor for photodegradation experiments. Two UV lamps with an intensity of 3.0 ± 0.1 mW/cm^2 were placed 20 cm from the photochemical reactor. The photodegradation efficiency was calculated using the following equation:

$$\text{Decolorization efficiency}\ (\%) = \frac{C_0 - C_i}{C_0} \times 100\% \quad (1)$$

where C_0 is the initial concentration of the dye and C_i is the final concentration of the dye after UV-vis irradiation for 60 min. The solution was placed in a centrifuge to separate the dye solution and sample after the photodegradation test. The final dye concentration was analyzed using a UV-vis spectrophotometer (Thermo Genesys-20), where λ was 590 nm for CV and 621 nm for MG.

For aqueous As^{5+} (H_3AsO_4; Merck), adsorption tests were performed using a similar process to that mentioned in the preceding section. Specifically, 40 mg of the sample and 5–25 ppm of aqueous As^{5+} were mixed in a 100-mL reactor in a dark environment for 60 min. After the adsorption tests, the concentration of the solution was determined using an inductively coupled plasma-optical emission spectrometry instrument (Agilent 5110).

Results and discussion

Physical and chemical properties of synthetic samples

Figure 1 presents the analysis results obtained for the crystal phase of the TNTs and AgTs samples. The results for the crystal phase of the TNTs were similar to those for the anatase phase of TiO_2. The AgTs included a AgCl crystal phase, an anatase phase, and a small amount of Ag. Peaks were observed at 25.27° and 48.0°, corresponding to the (101) and (200) planes of the anatase phase of TiO_2, respectively (JCPDS No. 21-1272). In addition, peaks were observed at 27.8°, 32.2°, 46.2°, 54.8°, and 57.5°, corresponding to the (111), (200), (220), (311), and (222) planes of the cubic phase of AgCl, respectively (JCPDS No. 31-1238). Another peak was observed at 38.2° that should be indexed to the Ag cubic phase (111) plane (JCPDS No. 65-2871). These results indicate that the amount of cubic phase Ag was very low in the Ag-modified TNTs sample. Ohno et al. (2001) reported that the anatase-to-rutile phase ratio in Degussa P-25 TiO_2 was approximately 75:25. The XRD data obtained for the resulting samples revealed that the rutile phase in raw P-25 TiO_2 was destroyed after the hydrothermal synthesis process. Several reports have indicated that the crystal phase TNTs sample exhibited an amorphous phase after the hydrothermal process. In general, if the crystal composition of TNTs transitions from the amorphous to the anatase or rutile phase, calcination must be performed to develop photocatalytic activities. However, after calcination, over conversion may induce the transformation of nanotubular structures into nanoparticles. This would considerably reduce the surface area of TNTs and then reduce the activated and adsorption sites. The XRD patterns presented herein indicates that our method can enable the preparation of AgTs without calcination or reduction treatment.

The total surface area (S_{BET}) and total pore volume (V_{total}) of a raw P-25 precursor were approximately 55 m^2/g and 0.15 cm^3/g, respectively. The S_{BET}, V_{total}, and pore size of the TNTs sample fabricated through hydrothermal synthesis

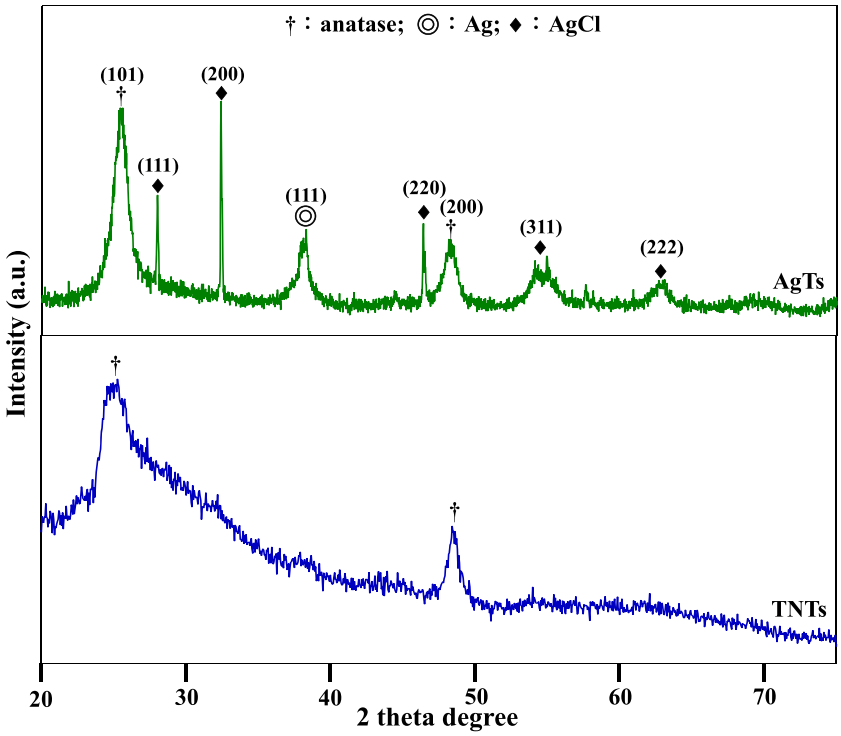

Fig. 1 XRD patterns of AgTs and TNTs samples

were approximately 392 m^2/g, 1.13 cm^3/g, and 11.5 nm, respectively. The surface area of the TNTs increased by nearly seven times compared with that of raw P-25. By contrast, the addition of Ag_2O markedly reduced the surface area of the as-prepared samples. Compared with the TNTs, the AgTs exhibited a significant reduction in S_{BET}, V_{total}, and pore size, with the corresponding values being approximately 261.8 m^2/g, 0.61 cm^3/g, and 9.3 nm, respectively. These results are similar to those in a previous study (Yee et al. 2017), which reported that precipitations blocked the ends of nanotubes and prevented the agglomeration and growth of Ag nanoparticles, resulting in a surface area reduction.

Figure 2 presents the N_2 adsorption/desorption isotherms and pore size distribution of the resulting TNTs and AgTs samples. As revealed by the isotherms, adding the Ag_2O precursor engendered significant changes in physical characteristics. We observed adsorption hysteresis for the samples when the relative pressure was higher than 0.6, signifying a type IV isotherm pattern (IUPAC classifications) (Gregg and Sing 1982; Sing 1985). Mogilevsky et al. (2008) reported that rolling up a nanosheet could result in the formation of a tubular shape. Hysteresis was observed because the plate-like or sheet-like aggregates resulted in slit-shaped pores (Kubo and Nakahira 2008). The pore volume of the TNTs sample was 1.2 $cm^3\ g^{-1}\ nm^{-1}$ at 2.2 nm. The volume increased to 1.4 $cm^3\ g^{-1}\ nm^{-1}$ (at 1.1 nm) when Ag_2O was added as a precursor. The pore size distribution of the AgTs sample became narrower than that of the TNTs sample. These results indicate that the properties of the precursor can strongly influence the porous structure of synthetic TNTs.

Figure 3 presents the synthesized samples' morphology observed using a TEM and HR-TEM. Compared with the AgTs sample, the TNTs sample exhibited a clearer tubular design. After the Ag_2O precursor was added, certain tubular and polygonal objects could be observed, as revealed by the TEM images. By observing the HR-TEM images, we determined d-spacing values of 0.35, 0.27, and 0.23 nm, corresponding to anatase (101), AgCl (200), and Ag (111), respectively.

Figure 4 depicts the SEM images. As revealed by the images, the samples showed a nanotubular shape. Moreover, Fig. 4 presents elemental EDS mapping results. The EDS results revealed the existence of Ti, O, Ag, and Cl in the TNTs and AgTs samples. Additionally, the EDS results indicated that Ag and Cl were homogeneously placed on the surface of the AgTs sample.

The absorption edges of the TNTs and AgTs were measured using a UV-vis spectrophotometer (Fig. 5). The literature values for Ag_2O and P-25 were 1.4 eV (Chen et al. 2016) and 3.27 eV (Pennington et al. 2018), respectively. The absorption edge of the TNTs sample was at approximately 365 nm (3.39 eV). The adsorption edge of the AgTs sample exhibited a blue shift, which was at approximately 300 nm (4.13 eV). This is because the band gap of AgCl is 5.6 eV (Zhao et al. 2015). This observation suggests that the junction formed between AgCl and the TNTs surface changed the band structure of the AgTs sample.

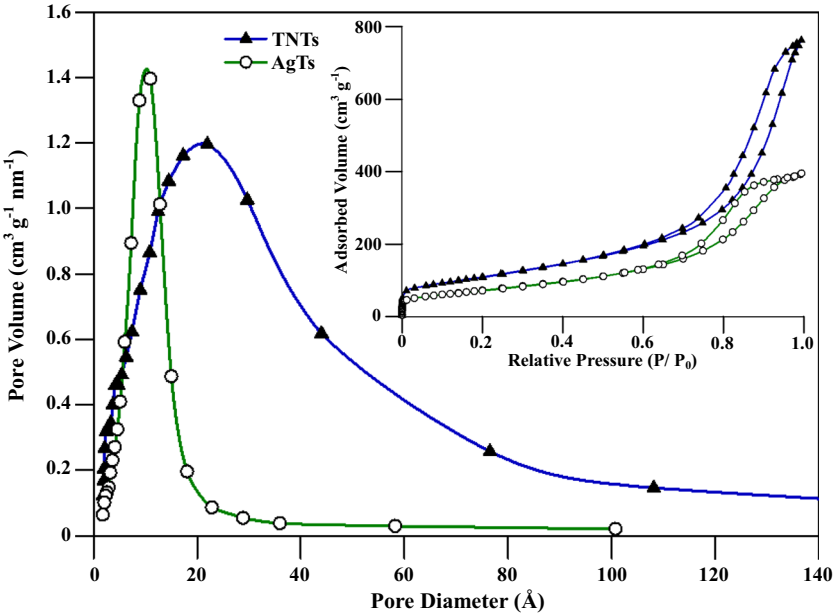

Fig. 2 N_2 adsorption/desorption isotherms and pore size distribution of resultant samples

PL spectroscopy was conducted on the as-prepared samples to determine the e^-/h^+ separation efficiency (Fig. 6). In general, three types of physical properties could be determined from the PL spectra of anatase TiO_2, namely, self-trapped excitons (Tang et al. 1993; Saraf et al. 1998), oxygen vacancies (Vo) (Saraf et al. 1998; Serpone et al. 1995), and surface states (Forss and Schubnell 1993). Three significant peaks could be observed at approximately 376, 466, and 561 nm. We attributed the peak at approximately 376 nm to the presence of self-trapped excitations from TiO_6^{8-} octahedrons (Tang et al. 1994). Saraf et al. (1998) and Serpone et al. (1995) have reported that the PL spectra of anatase TiO_2 revealed a peak at the long wavelength side, which was attributed to Vo. Additionally, the PL spectra revealed shallow traps at 0.51 eV (465 nm) (Serpone et al. 1995) and 0.8 eV (525 nm) (Saraf et al. 1998) below the conduction band (CB), which were attributed to Vo. In the current study, the peak at approximately 466 nm was considered to indicate the existence of surface defects and was attributed to Vo. Other studies have indicated that the peak at 525 nm signified a trap with Ti atoms adjacent to Vo (Redmond et al. 1993; Lei et al. 2001). In our PL spectra, no peak was observed at 525 nm, indicating that most e^- elements were trapped by the oxygen vacancy. The oxygen vacancy sites were positive, which favored the adsorption of anions (Oikawa and Takamura 2015). The emission peak at about 561 nm was assigned to the irradiative recombination of charge carriers (Knorr et al. 2008). Tang et al. (1994) indicated that PL emission intensity is the result of the recombination of moved e^-/h^+ by PL emission. Therefore, an increase in e^-/h^+ separation would be observed at a lower PL intensity of the sample. The PL results demonstrated that the addition of Ag_2O as a precursor reduced the e^-/h^+ recombination rate compared with that for the non-modified TNTs. Anion species or metals (e.g., Cl, Sn, and

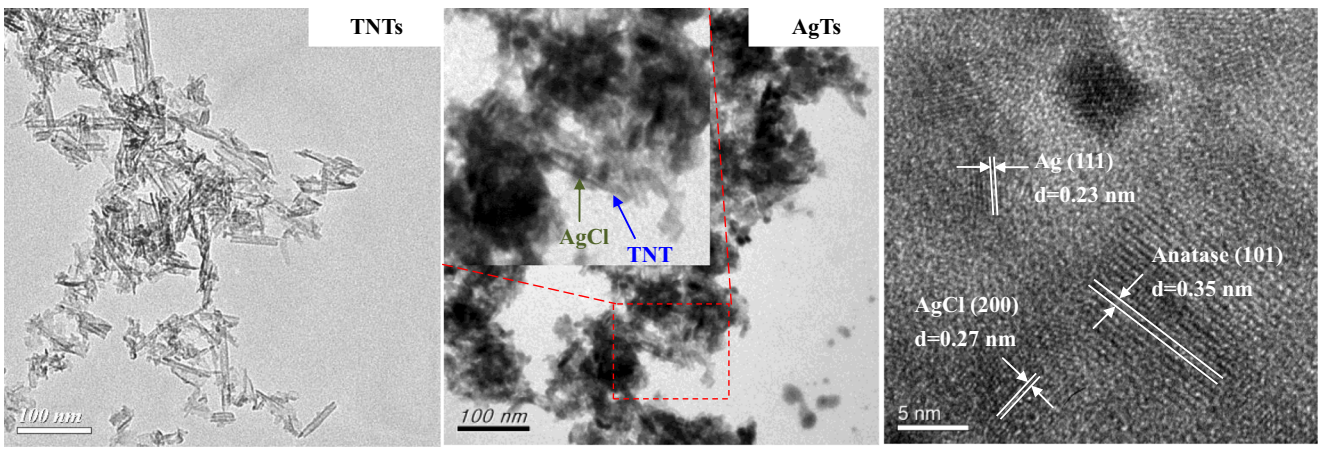

Fig. 3 TEM and HR-TEM images of TNTs and AgTs samples

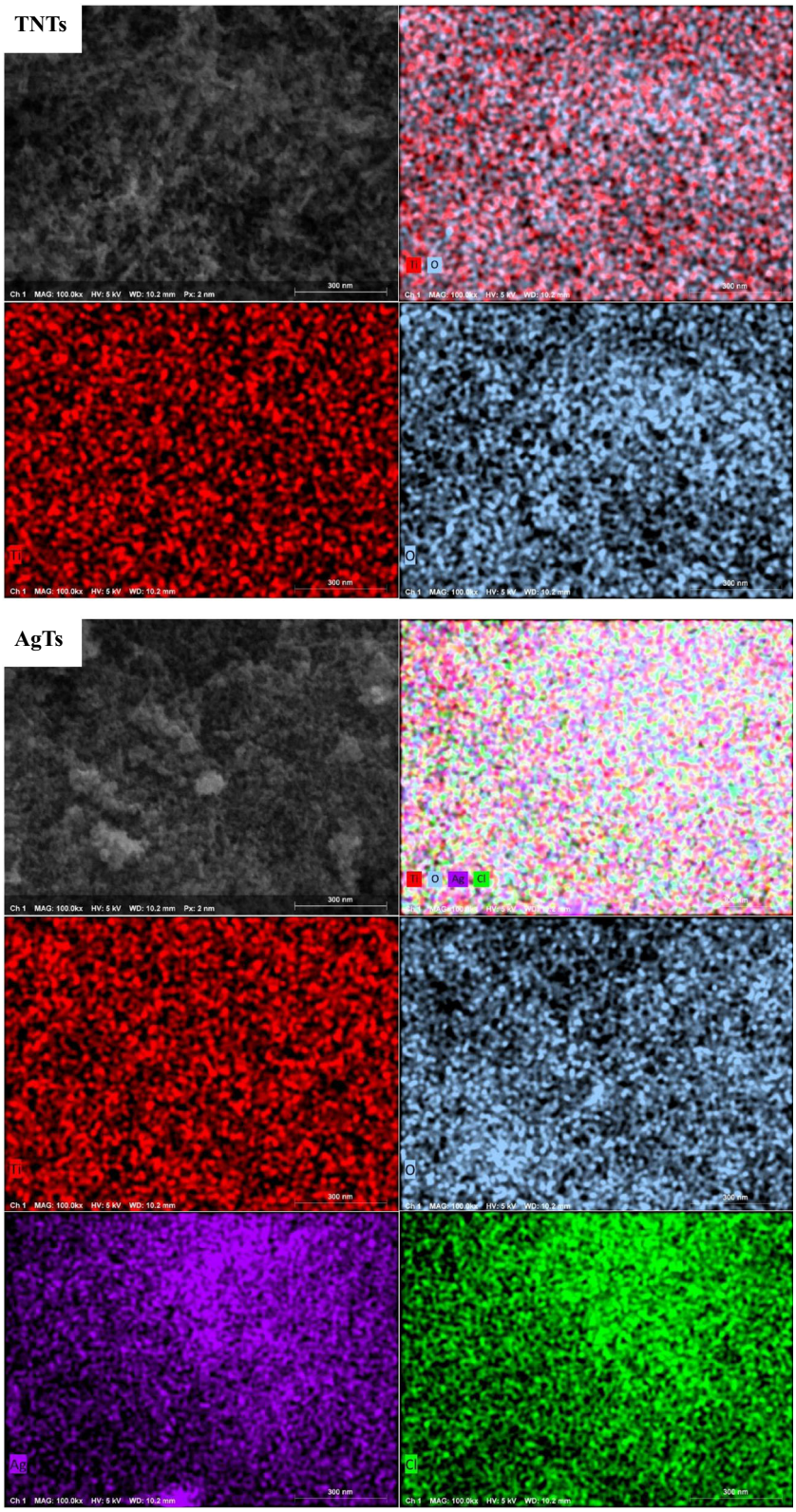

Fig. 4 SEM and EDS images of synthesized samples

Ag) having small resistance can conduct electrons (Elahifard et al. 2007; Kowalska et al. 2009; Yu and Jimmy 2009); therefore, the electron-hole recombination rate is reduced. Moreover, some studies have suggested the loading of Ag nanoparticles on the surface of TiO_2. A heterojunction (Schottky junction) would be created between Ag and TiO_2,

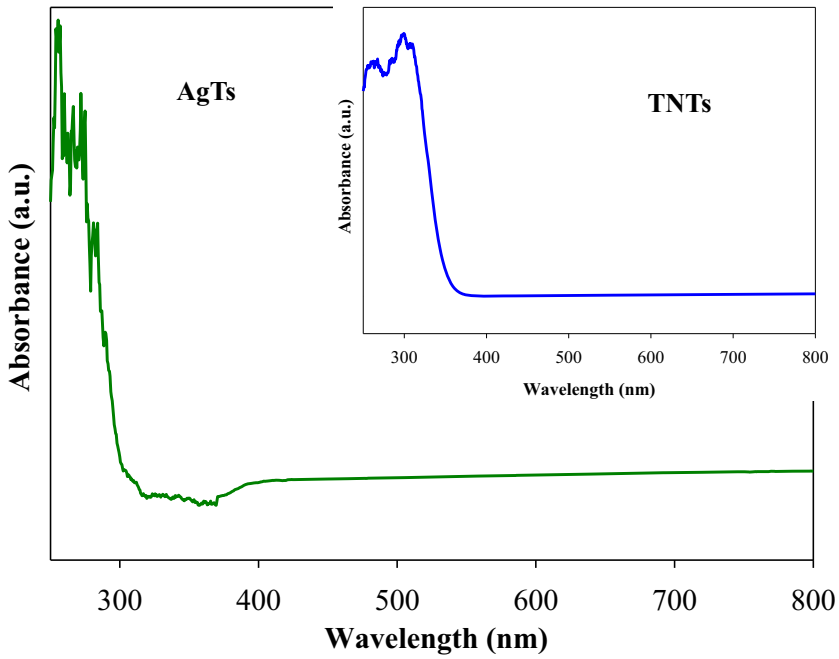

Fig. 5 UV-vis spectra of resultant samples

with CB electrons being shifted to the Ag clusters because of the higher work function of Ag, thus effectively restraining the recombination of e^-/h^+ pairs (Wold 1993; Linsebigler et al. 1995; He et al. 2011a).

Figure 7 illustrates the XPS spectra of Ti, O, and Ag of the as-prepared samples. Magnified peaks, namely Ti^{4+} and Ti^{3+}, were observed, signifying the presence of TiO_2 and Ti_2O_3, respectively (Borges et al. 2008; Gharagozlou and Bayati 2014). The primary reason for the reduction of Ti^{4+} to Ti^{3+} was the presence of the oxygen vacancy (Borges et al. 2008). The O1s spectra of the samples exhibited a wide and asymmetric shape, indicating the presence of two chemical states. The O1s peak of the samples contained two constituents, namely hydroxyl groups (–OH) and lattice oxygen (Ti–O).

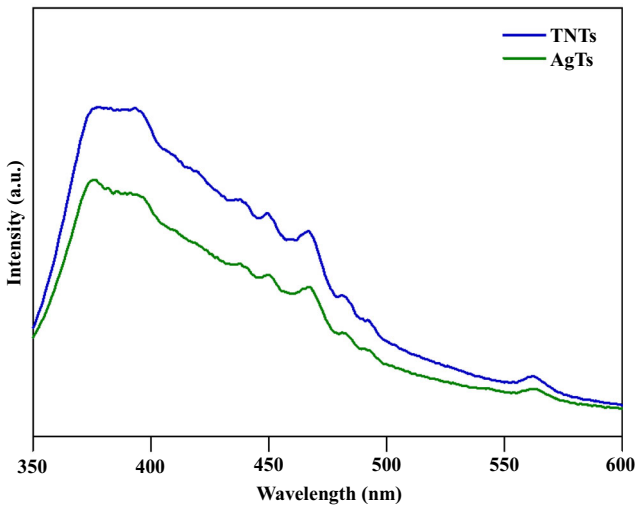

Fig. 6 Photoluminescence spectra of fabricated TNTs and AgTs samples

The patterns showed a primary peak, which was ascribed to the Ti–O bonds in the TiO_6^{8-} octahedral crystal lattice, and a secondary peak, which was ascribed to –OH attached to the upper layer of the surface (Wang et al. 2012). Furthermore, two peaks were noted between 376 and 364 eV, which were attributed to the spin-orbit splitting of $3d_{3/2}$ and $3d_{5/2}$ of Ag, respectively. These peaks could be further separated into two peaks, namely Ag^+ of AgCl andAg^0 (Huang et al. 2015).

Vapor-phase elemental mercury removal experiments

Figure 8 presents the Hg breakthrough curves of the TNTs and AgTs under UV irradiation or darkness in a N_2 environment. The AgTs exhibited a higher level of photodegradation efficiency than did the TNTs sample. Under UV irradiation, the Hg^0 removal efficiency levels increased sharply at runs 16–30 and 41–50, revealing that the inlet Hg^0 was removed through the adsorption and oxidation function of the sample. The notable increase in Hg^0 degradation for the samples validates the crucial role of the synthesized samples in the photocatalysis of oxide Hg^0 into Hg^{2+}, thereby increasing the removal of gas-phase Hg species. The Hg^0 removal efficiencies of the AgTs and TNTs samples were approximately 86.1% and 62.9%, respectively (run 30). The surface area of the materials increased with the content of active sites. The S_{BET} and V_{total} values of the TNTs sample were 392 m^2/g and 1.13 cm^3/g, respectively, which were higher than those of the AgTs sample (261.8 m^2/g and 0.61 cm^3/g, respectively). However, the AgTs presented superior Hg^0 removal efficiency, which can be attributed to the sufficient separation of e^-/h^+ pairs and oxygen vacancies, corresponding to the aforementioned sample

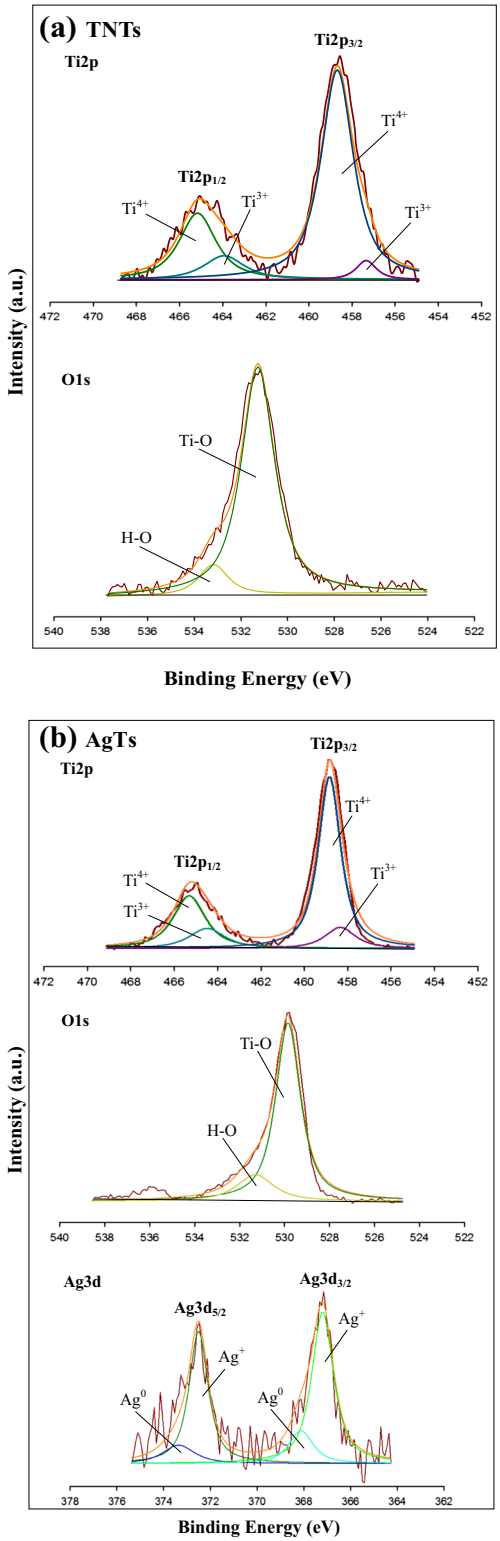

Fig. 7 XPS spectrums of synthesized samples

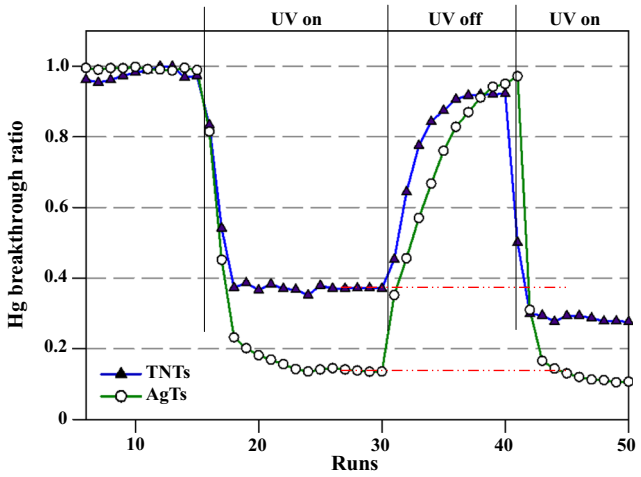

Fig. 8 Hg^0 breakthrough behaviors for TNTs and AgTs samples

analysis results. The species of theTiO_2 surface could act as rapid reaction media (e.g., OH radicals), thus improving the photodegradation efficiency of the AgTs sample. Several studies have indicated that primary oxides, such as OH• were produced through the oxidation of H_2O adsorbed on TiO_2, and the produced OH• subsequently oxidized the contaminant (Jain et al. 2007; Xiao et al. 2008). In the current study, the Hg removal efficiency observed at runs 41–50 was higher than that observed when UV irradiation was first applied (runs 16–30). A similar phenomenon has been observed is previous studies because Hg^0 was removed using photocatalysis and adsorption simultaneously (Wu et al. 1998; Pitoniak et al. 2003; Wang et al. 2011). Therefore, the Hg^0 removal efficiencies observed at later runs were superior to those obtained when UV irradiation was first applied.

According to the findings of this study as well as the mechanisms proposed in previous studies (Chen et al. 2014; Anpo 2004; Pal and Ariya 2004; Li and Wu 2006, 2007; Lee and Hyun 2006; Wang et al. 2010), the possible degradation mechanisms of Hg^0 on the surface of AgTs, including oxidation and adsorption, are illustrated in Fig. 9. In a gas-phase Hg^0 mixed N_2 environment, TNTs primarily rely on a low concentration of $O_2^{\bullet-}$ and OH•, which can be generated by the pre-adsorbed H_2O and O_2 on the TNTs surface for the photocatalytic oxidation of Hg^0. Moreover, the oxygen vacancies and defect sites on the TNTs surface can enhance the oxidation of Hg^0 into Hg^{2+}. The surface functional groups of TNTs, for example Cl species and oxygenated groups, can simply adsorb Hg^0. Because Hg^0 and HgO have strong affinity, the adsorbed oxidized Hg (i.e., HgO) on the TNTs surface can further adsorb Hg^0. Furthermore, Hg^0 can be oxidized by Cl_2 and $\bullet ClOH^-$, which can be formed through a reaction between Cl^-, OH•, and h^+ (Zhao et al. 2014), and h^+ can increase the oxidation of Cl^- to Cl^0 atoms because of the negatively charged AgCl surface (Tian et al. 2014). The formed Cl^0 atoms can oxidize Hg^0 into Hg^{2+} because of the high oxidation ability of Cl^0 and can be reduced to Cl^- ions again to react with Ag^+ in order to maintain the steadiness of AgCl (Tian et al. 2014; Zhao and Hao 2014). On the basis of the photocatalytic reaction,

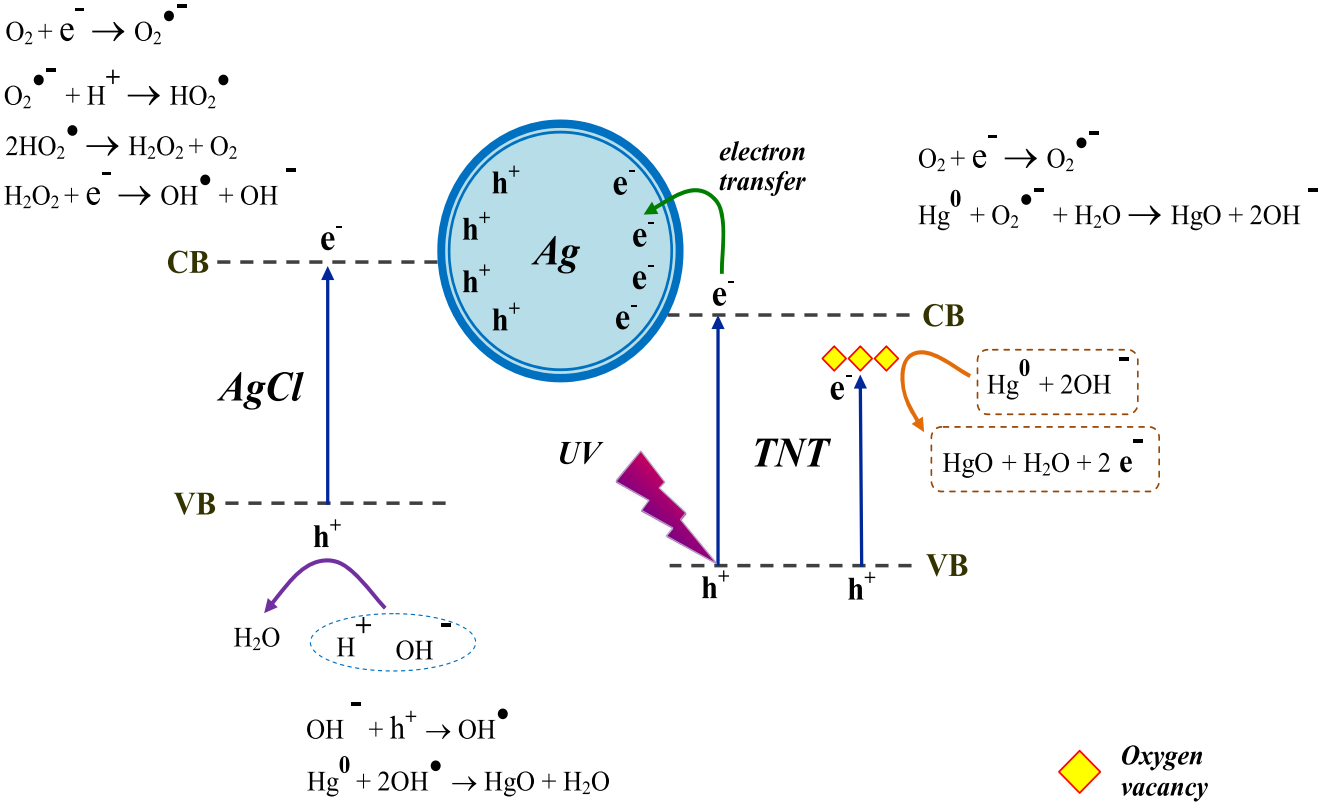

Fig. 9 Hg^0 oxidation and adsorption mechanisms for AgTs

reactive substances including OH•, $O_2^{\bullet -}$, h^+, and Cl^0 can strongly oxidize Hg^0.

Photodecomposition of dyes

CV and MG were employed to measure the photocatalytic activities and adsorption efficiencies of the as-prepared samples under UV irradiation and dark conditions, respectively. Figure 10 illustrates the CV and MG photodegradation efficiency levels. The dye photodecomposition efficiency of the AgTs heterostructures was superior to that of the TNTs sample. The CV and MG removal efficiency levels of the AgTs sample were 56.57% and 71.65%, respectively. By contrast, the TNTs sample had lower CV and MG removal efficiency levels, namely 48.86% and 67.77%, respectively. Notably, the S_{BET} and V_{total} values of the AgTs were lower than those of the TNTs sample. The MG removal efficiency of both samples was higher than the CV removal efficiency, and the primary reason for this may be that the molar mass of MG (364.91 g/mol) is lower than that of CV (407.99 g/mol). For the same photocatalyst and test condition, the MG photodegradation efficiency was higher than the CV photodegradation efficiency. This finding suggests that photocatalytic activity was enhanced through Ag modification, which increased the separation efficiency of e^-/h^+ pairs. Furthermore, discussing the dye adsorption efficiency levels of the synthesized samples under dark conditions is crucial. The CV adsorption efficiency levels of the AgTs and TNTs were 15.98% and 6.16%, respectively. The AgTs had a smaller S_{BET} than did the TNTs sample; however, the CV adsorption efficiency of the AgTs was superior to that of the TNTs sample. This superiority may be attributed to the presence of Cl^- in CV dye (Fig. 10). Therefore, it can be adsorbed easily on the oxygen vacancy sites of the AgTs sample. By contrast, the MG adsorption efficiency did not differ significantly between the samples (1.83% for the TNTs and 1.62% for the AgTs) because of the absence of Cl^-. Therefore, the adsorption efficiency of MG depends on surface area of sample. These results suggest that the surface of AgTs has more oxygen vacancy sites compared with that of TNTs. In addition, the photodecomposition efficiency of MG with L-ascorbic acid addition significantly decreased to 44.91% (AgTs) and 38.33% (TNTs), which reduction one of fourth compares with that of MG + UV. The results suggested that oxidizing radical is one of the key factors for driving the photodecomposition dye.

The test results indicated that the formations of most dyes were degraded by the photocatalytic function of the synthesized samples. The primary reaction processes of TiO_2 under UV irradiation are summarized by the following equations (Giménez et al. 1997; San et al. 2002; da Silva and Faria 2003; Akpan and Hameed 2009; Wang et al. 2009; Xin et al. 2009):

$$TiO_2 + hv \rightarrow e^- + h^+ \quad (2)$$

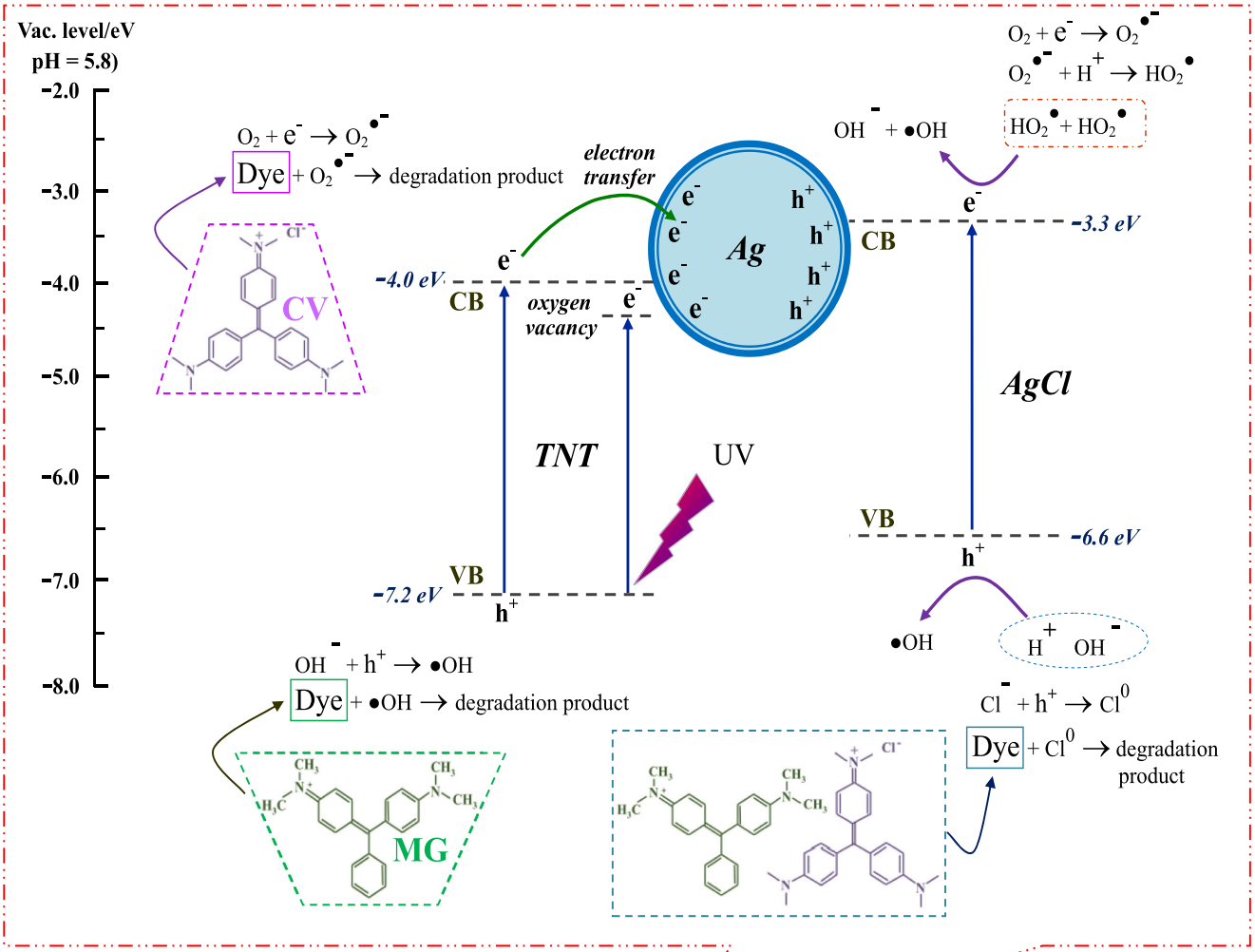

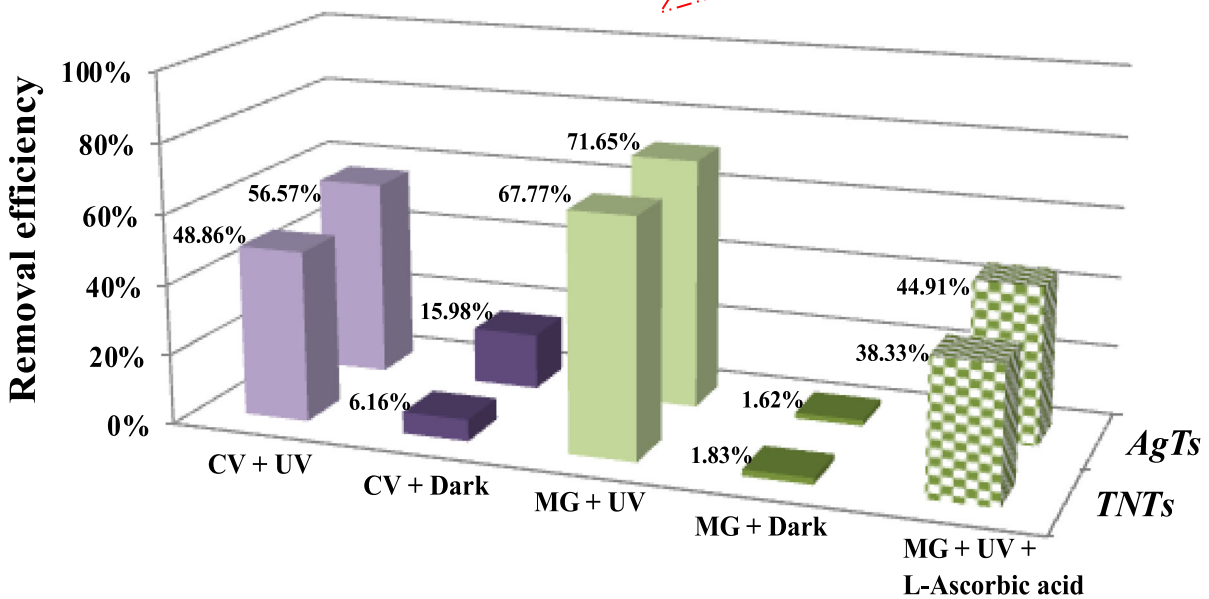

Fig. 10 Photocatalytic degradation of dyes of fabricated samples and removal mechanisms for AgTs sample

$$e^- + O_2 \rightarrow {}^{\bullet}O_2^- \quad (3)$$

$$2HOO^{\bullet} \rightarrow H_2O_2 + O_2 \quad (4)$$

$$H_2O_2 + e^- \rightarrow {}^{\bullet}OH + OH^- \quad (5)$$

$$h^+ + H_2O_{(ads)} \rightarrow {}^{\bullet}OH + H^+ \quad (6)$$

$$\text{Dye} + {}^{\bullet}OH\ (\text{or}\ {}^{\bullet}O_2^-) \rightarrow \text{degradation product} \quad (7)$$

According to Eqs. (2)–(7) and the experimental results, the dye degradation process of the AgTs can be explained by the following mechanism (Fig. 10). Photogenerated e^-/h^+ pairs can be created on the AgTs surface under UV irradiation. The photogenerated electrons can then be transferred to TiO_2, whereas holes can be transferred to AgCl because of the suitable CB and valence band energy levels between AgCl (− 3.3 V and − 6.6 eV) and TiO_2 (− 4.0 V and − 7.2 eV). Consequently, the recombination rate of the photogenerated e^-/h^+ pairs can be reduced (Morimoto et al. 2007; Tian et al. 2014). Moreover, a heterojunction between Ag and TiO_2 can hinder the recombination of e^-/h^+ pairs (Wold 1993; Linsebigler et al. 1995; He et al. 2011a). In addition to ${}^{\bullet}O_2^-$ and ${}^{\bullet}OH$ (Eqs. (3), (5), and (6)), the h^+ coupled with Cl^- may produce Cl^0 radicals. The decomposition of organic dyes can also be achieved through Cl^0 radicals (Eqs. (8) and (9)) (Yu et al. 2009).

$$Cl^- + h^+ \rightarrow Cl^0 \quad (8)$$

$$\text{Dye} + Cl^0 \rightarrow \text{degradation product} \quad (9)$$

In the reaction environment, active species including ${}^{\bullet}O_2^-$, ${}^{\bullet}OH$, and Cl^0 precipitate during the mineralization and decomposition of dyes.

Arsenate adsorption tests

Adsorption isotherm model is beneficial to predict the adsorption amount of materials. Two popular models were utilized to describe adsorption between sample and As^{5+}, which are Langmuir and Freundlich. The linear forms of Langmuir (Eq. (10)) and Freundlinch (Eq. (11)) models are present as follows:

$$\frac{C_e}{q_e} = \frac{1}{(q_{\max})b} + \frac{C_e}{q_{\max}} \quad (10)$$

$$\log q_e = \log K_f + \frac{1}{n}\log C_e \quad (11)$$

For the Langmuir isotherm, C_e and q_e are the equilibrium concentration of As^{5+} (mg L^{-1}) and the amount of adsorbate adsorbed (As^{5+}) per unit of mass of adsorbent (mg g^{-1}), respectively. And $q_{\max}$ is the monolayer maximum adsorption capacity (mg g^{-1}) and b is the constant of Langmuir. For the Freundlich adsorption model, K_f is associated to adsorption amount (mg g^{-1}) as well as $1/n$ is an estimate of adsorption intensity and surface heterogeneity.

The isotherm models of sample with As^{5+} are shown in Fig. 11 (a) Langmuir and (b) Freundlich. For TNTs sample, adsorption data of As^{5+} more fit well with Langmuir (R^2 = 0.9940) that compared to Freundlich (R^2 = 0.9550) equation. In contrast, AgTs sample fit well with both models, which R^2 values are 0.9941 (Langmuir) and 0.9988 (Freundlich). The theoretical calculated $q_{\max}$ of TNT and AgTs for As^{5+} is 15.38 and 21.10 mg g^{-1}, respectively.

In the dark environment, the adsorption of arsenate on the TiO_2 surface occurred only through electrostatic factors. Equations (12)–(14) demonstrate $H_2AsO_4^-$ to be the predominant As^{5+} species (Goldberg and Johnston 2001; Dutta et al. 2004; Sharma and Sohn 2009; Rivera-Reyna et al. 2013).

$$H_3AsO_4 \leftrightarrow H^+ + H_2AsO_4^- \qquad pK_1 = 2.3 \quad (12)$$

$$H_2AsO_4^- \leftrightarrow H^+ + HAsO_4^{2-} \qquad pK_2 = 6.8 \quad (13)$$

$$HAsO_4^{2-} \leftrightarrow H^+ + AsO_4^{3-} \qquad pK_3 = 11.6 \quad (14)$$

He et al. (2011b) indicated that the surface functional groups (–H_2O and –OH) on the surface of TiO_2 with arsenate species can form inner-sphere arsenate complexation through the ligand exchange of unprotonated oxygen atoms. Wei et al. (2011) applied density functional theory to calculate As^{5+} on the TiO_2 anatase (101) plane. They concluded that the order of adsorption abilities for arsenate species, water, and OH^- was as follows: $AsO_4^{3-} > OH^- > HAsO_4^{2-} > H_2AsO_4^- > H_3AsO_4 > H_2O$ (Wei et al. 2011). The aforementioned studies have indicated that TiO_2 first adsorbs OH^- firstly, and then generates complexation through a ligand exchange of $H_2AsO_4^-$ or $HAsO_4^{2-}$.

Arsenate species on the TiO_2 surface form complexation through the monodentate mononuclear (MM) complex, which can theoretically increase the amount of arsenate adsorbed on the TiO_2 surface because it occupies one surface Ti site. Wei et al. (2016) indicated that because one H-bond between $HAsO_4^{2-}$ and surface O cannot generate a steady MM structure, two H-bonds are required to form the MM structure in order to achieve structural stability. Therefore, although the mechanism of the adsorption of $HAsO_4^{2-}$ on the TiO_2 surface was first determined to be an MM complex, it should shift to a bidentate binuclear (BB) complex. Moreover, regarding adsorption energy, the BB surface complex was the most thermodynamically favorable mode at low pH (He et al. 2009). The amount of arsenate species adsorbed decreased with the generation of the BB type (Wei et al. 2016). Jegadeesan et al. (2010) utilized X-ray absorption near-edge structure and extended X-ray absorption fine structure to measure the

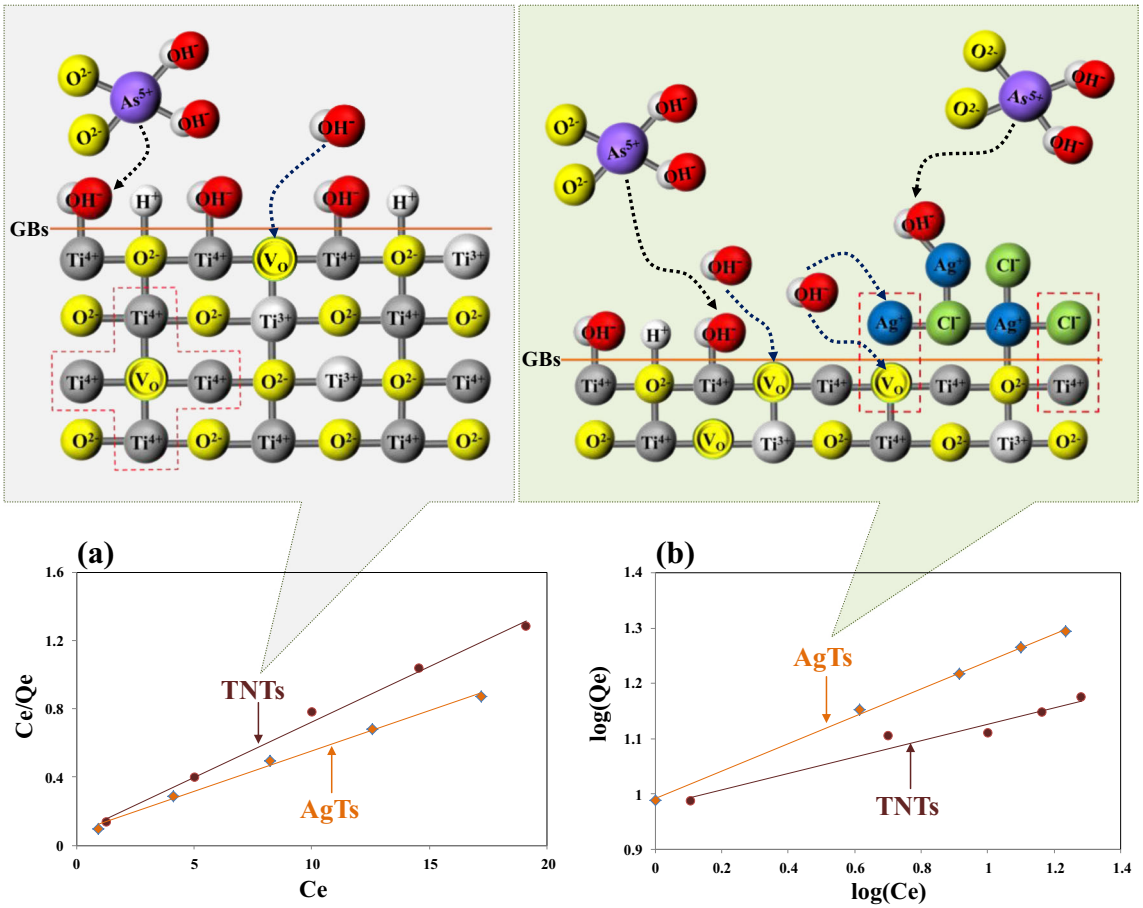

Fig. 11 Arsenate adsorption mechanisms and (**a**) Langmuir and (**b**) Freundlich adsorption isotherms

mechanisms of arsenate adsorption on TiO_2; they reported that the mechanism of the adsorption of As^{5+} on commercial crystalline TiO_2 was also a characteristic of a BB complex.

According to the arsenate species adsorption test and the observed physical characteristics of the resultant samples, we developed a sample surface structure for explaining the adsorption behavior of arsenate species (Fig. 11). In this study, the O and Ti sites of the TNTs surface adsorbed H^+ and OH^-, respectively. The PL and XPS Ti2p analysis indicated the existence of an oxygen vacancy (Vo) in the synthesized samples. Because the TNTs shape was formed in a strong alkaline solution, planar defects may be created with the Ti–O–Ti linkages of the octahedrons coordinated TiO_2 break. A previous study suggested that oxygen vacancies can be easily created in grain-boundaries (GBs) (Ihara et al. 2003). Wendt et al. (2005) reported oxygen vacancies to be major reactive agents for various adsorbents; therefore, several reactions on the adsorbent surface could be affected by these point defects. Because of the existence of oxygen vacancies around Ti^{4+}, such sites were determined to possess positive charges that can be beneficial for the attraction of OH^- (Wendt et al. 2005). Arsenate species could engage in ligand exchanges with OH^- on the TiO_2 surface to generate complexation. Dye photodegradation and gas-phase Hg^0 removal tests suggested that AgCl and TiO_2 formed a heterojunction, thus effectively blocking the recombination of e^-/h^+ pairs. Therefore, the AgTs had superior photodecomposition efficiency, although the BET of the AgTs was smaller than that of the TNTs. For the AgTs sample, in addition to Ti and oxygen vacancy sites bonding with OH^-, the sites around Ti^{4+} with Cl^- may also possess positive charges. In addition, the Ag_2O phase was not determined in the XRD pattern, indicating that most of the oxygen sites between AgCl and TNTs were vacant. Accordingly, we infer that AgTs can absorb more arsenate species than can TNTs.

Conclusions

In this study, AgTs were successfully synthesized through a hydrothermal process without additional calcination or reduction treatment. We compared a TNTs sample with the AgTs sample, and we observed that the TNTs sample had a larger BET surface (392 m^2/g) than did the AgTs sample. The crystal phase of the AgTs sample was the anatase phase, cubic AgCl, and Ag coexistence. The unmodified TNTs had a nanotubular shape, and the AgTs exhibited certain tubular shapes and some

polygonal shape. PL and XPS results indicate that the pre-adsorbed H_2O, OH groups, and oxygen vacancies were on the surfaces of the synthesized samples. The e^-/h^+ pair separation time was enhanced by the presence of Ag and AgCl species on the surface of the AgTs, which has benefits to generate more $^{\bullet}O_2^-$ and $^{\bullet}OH$. AgTs is a high performance absorbent due to without calcination treatment. Moreover, AgTs also has a multiple function of photocatalyst because of e^-/h^+ pair recombination reduction. Therefore, AgTs can achieve outstanding adsorption and oxidation functions for vary contaminants. Containing C–H organic pollutant, such as dye in this study, can be degraded by the $^{\bullet}O_2^-$ and $^{\bullet}OH$ on AgTs surface. On the other hand, containing Cl^- ion CV dye is easily adsorbed on the AgTs sample, which indirectly proves AgTs sample possesses more oxygen vacancy sites. For the inorganic contaminants, such as As^{5+}, AgTs remove it mostly through adsorptions. Since As^{5+} adsorption is mainly by ligand exchange with OH^- on the sample surface, hence more oxygen vacancy site has a high affinity to absorb As^{5+}. In contrast, vapor-phase Hg^0 removal process is not like As^{5+} only by adsorption removal because Hg^0 is not easily captured by adsorbents. AgTs first oxidize Hg^0 into HgO, and then HgO adsorbs on AgTs surface to achieve better removal efficiency. In addition, the oxidation of Hg^0 can be enhanced by the oxygen vacancy and defect sites on the AgTs surface. When HgO was formed and adsorbed on the AgTs surface, Hg^0 can be further adsorbed on the AgTs surface because Hg^0 and HgO have strong affinity. Oxidation and adsorption are both important functions for the vapor-phase Hg^0 removal. Overall, the AgTs sample was determined to possess superior CV and MG photodegradation efficiency levels compared with the unmodified TNTs sample. Oxygen vacancy sites on the AgTs sample were determined to be advantageous for As^{5+} adsorption. Furthermore, Hg^0 removal relies on AgTs outstanding oxidation and adsorption abilities.

Acknowledgments The authors specially acknowledge Ms. Ya-Yun Yang and Ms. Ching-Yen Lin of Ministry of Science and Technology (National Taiwan University) for their technical assistance in FE-SEM and TEM experiments.

Funding information This research was financially supported by the Ministry of Science and Technology, Taiwan under grant no. 103-2313-B-002-018-MY3 and 106-2313-B-002-006-MY3.

References

Abukhadra MR, Adlii A, Bakry BM (2019) Green fabrication of bentonite/chitosan@cobalt oxide composite (BE/CH@Co) of enhanced adsorption and advanced oxidation removal of Congo red dye and Cr(VI) from water. Int J Biol Macromol 126:402–413

Abukhadra MR, Shaban M, Sayed F, Saad I (2018) Efficient photocatalytic removal of safarnin-O dye pollutants from water under sunlight using synthetic bentonite/polyaniline@Ni_2O_3 photocatalyst of enhanced properties. Environ Sci Pollut Res 25:33264–33276

Akpan UG, Hameed BH (2009) Parameters affecting the photocatalytic degradation of dyes using TiO_2-based photocatalysts: a review. J Hazard Mater 170:520–529

Anpo M (2004) Preparation, characterization, and reactivities of highly functional titanium oxide-based photocatalysts able to operate under UV–visible light irradiation: approaches in realizing high efficiency in the use of visible light. Bull Chem Soc Jpn 77:1427–1442

Bavykin DV, Friedrich JM, Walsh FC (2006) Protonated titanates and TiO_2 nanostructured materials: synthesis, properties, and applications. Adv Mater 18:2807–2824

Bavykin DV, Lapkin AA, Plucinski PK, Friedrich JM, Walsh FC (2005) Reversible storage of molecular hydrogen by sorption into multilayered TiO_2 nanotubes. J Phys Chem B 109:19422–19427

Borges ME, Alvarez-Galván MC, Esparza P, Medina E, Martín-Zarza P, Fierro JLG (2008) Ti-containing volcanic ash as photocatalyst for degradation of phenol. Energy Environ Sci 1:364–369

Chen SS, Hsi HC, Nian SH, Chiu CH (2014) Synthesis of N-doped TiO_2 photocatalyst for low-concentration elemental mercury removal under various gas conditions. Appl Catal B 160:558–565

Chen YJ, Chiang YW, Huang MH (2016) Synthesis of diverse Ag_2O crystals and their facet-dependent photocatalytic activity examination. ACS Appl Mater Interfaces 8:19672–19679

da Silva CG, Faria JL (2003) Photochemical and photocatalytic degradation of an azo dye in aqueous solution by UV irradiation. J Photochem Photobio A 155:133–143

Dutta PK, Ray AK, Sharma VK, Millero FJ (2004) Adsorption of arsenate and arsenite on titanium dioxide suspensions. J Colloid Interface Sci 278:270–275

Elahifard MR, Rahimnejad S, Haghighi S, Gholami MR (2007) Apatite-coated Ag/AgBr/TiO_2 visible-light photocatalyst for destruction of bacteria. J Am Chem Soc 129:9552–9553

Forss L, Schubnell M (1993) Temperature dependence of the luminescence of TiO_2 powder. Appl Phys B Lasers Opt 56:363–366

Gharagozlou M, Bayati R (2014) Photocatalytic activity and formation of oxygen vacancies in cation doped anatase TiO_2 nanoparticles. Ceram Int 40:10247–10253

Giménez J, Curcó D, Marco P (1997) Reactor modelling in the photocatalytic oxidation of wastewater. Water Sci Technol 35:207–213

Goldberg S, Johnston CT (2001) Mechanisms of arsenic adsorption on amorphous oxides evaluated using macroscopic measurements, vibrational spectroscopy, and surface complexation modeling. J Colloid Interface Sci 234:204–216

Gregg SJ, Sing KSW (1982) Adsorption, surface area and porosity, 2nd edn. Academic Press, London

He G, Zhang M, Pan G (2009) Influence of pH on initial concentration effect of arsenate adsorption on TiO_2 surfaces: thermodynamic, DFT, and EXAFS interpretations. J Phys Chem C 113:21679–21686

He X, Cai Y, Zhang H, Liang C (2011b) Photocatalytic degradation of organic pollutants with Ag decorated free-standing TiO_2 nanotube arrays and interface electrochemical response. J Mater Chem 21:475–480

He G, Pan G, Zhang M (2011c) Studies on the reaction pathway of arsenate adsorption at water–TiO_2 interfaces using density functional theory. J Colloid Interface Sci 364:476–481

Hsi HC, Lee HH, Hwang JF, Chen W (2010) Mercury speciation and distribution in a 660-megawatt utility boiler in Taiwan firing bituminous coals. J Air Waste Manage Assoc 60:514–522

Hsi HC, Tsai CY (2012) Synthesis of TiO_{2-x} visible-light photocatalyst using N_2/Ar/He thermal plasma for low-concentration elemental mercury removal. Chem Eng J 191:378–385

Huang Z, Wen M, Wu D, Wu Q (2015) A special Ag/AgCl network-nanostructure for selective catalytic degradation of refractory chlorophenol contaminants. RSC Adv 5:12261–12267

Ihara T, Miyoshi M, Iriyama Y, Matsumoto O, Sugihara S (2003) Visible-light-active titanium oxide photocatalyst realized by an oxygen-deficient structure and by nitrogen doping. Appl Catal B 42:403–409

Jain R, Mathur M, Sikarwar S, Mittal A (2007) Removal of the hazardous dye rhodamine B through photocatalytic and adsorption treatments. J Environ Manag 85:956–964

Jegadeesan G, Al-Abed SR, Sundaram V, Choi H, Scheckel KG, Dionysiou DD (2010) Arsenic sorption on TiO_2 nanoparticles: size and crystallinity effects. Water Res 44:965–973

Kasuga T, Hiramatsu M, Hoson A, Sekino T, Niihara K (1999) Titania nanotubes prepared by chemical processing. Adv Mater 11:1307–1311

Knorr FJ, Mercado CC, McHale JL (2008) Trap-state distributions and carrier transport in pure and mixed-phase TiO_2: influence of contacting solvent and interphasial electron transfer. J Phys Chem C 112:12786–12794

Kowalska E, Abe R, Ohtani B (2009) Visible light-induced photocatalytic reaction of gold-modified titanium(IV) oxide particles: action spectrum analysis. Chem Commun 2:241–243

Kubo T, Nakahira A (2008) Local structure of TiO_2-derived nanotubes prepared by the hydrothermal process. J Phys Chem C 112:1658–1662

Lei Y, Zhang LD, Meng GW, Li GH, Zhang XY, Liang CH, Chen W, Wang SX (2001) Preparation and photoluminescence of highly ordered TiO_2 nanowire arrays. Appl Phys Lett 78:1125–1127

Lee TG, Hyun JE (2006) Structural effect of the in situ generated titania on its ability to oxidize and capture the gas-phase elemental mercury. Chemosphere 62:26–33

Linsebigler AL, Lu G, Yates JT (1995) Photocatalysis on TiO_2 surfaces: principles, mechanisms, and selected results. Chem Rev 95:735–758

Li Y, Cao X, Wang L, Wang Y, Xu Q, Li Q (2017) Light-induced deposition of Pd-based nanoalloy on TiO_2 nanotubes for formic acid electrooxidation. J Taiwan Inst Chem Eng 76:109–114

Li Y, Wu CY (2006) Role of moisture in adsorption, photocatalytic oxidation, and reemission of elemental mercury on a SiO_2−TiO_2 nanocomposite. Environ Sci Technol 40:6444–6448

Li Y, Wu CY (2007) Kinetic study for photocatalytic oxidation of elemental mercury on a SiO_2–TiO_2 nanocomposite. Environ Eng Sci 24:3–12

Mogilevsky G, Chen Q, Kleinhammes A, Wu Y (2008) The structure of multilayered titania nanotubes based on delaminated anatase. Chem Phys Lett 460:517–520

Mohamed F, Abukhadra MR, Shaban M (2018) Removal of safranin dye from water using polypyrrole nanofiber/Zn-Fe layered double hydroxide nanocomposites (Ppy NF/Zn-Fe LDH) of enhanced adsorption and photocatalytic properties. Sci Total Environ 640-641:352–363

Morimoto T, Suzuki K, Torikoshi M, Kawahara T, Tada H (2007) Ag (core)–AgCl (shell) standard microelectrode-loaded TiO_2. Chem Commun 41:4291–4293

Narayani H, Jose M, Sriram K, Shukla S (2018) Hydrothermal synthesized magnetically separable mesostructured $H_2Ti_3O_7$/γ-Fe_2O_3 nanocomposite for organic dye removal via adsorption and its regeneration/reuse through synergistic non-radiation driven H_2O_2 activation. Environ Sci Pollut Res 25:20304–20319

Ohno T, Sarukawa K, Tokieda K, Matsumura M (2001) Morphology of a TiO_2 photocatalyst (Degussa, P-25) consisting of anatase and rutile crystalline phases. J Catal 203:82–86

Oikawa I, Takamura H (2015) Correlation among oxygen vacancies, protonic defects, and the acceptor dopant in Sc-doped $BaZrO_3$ studied by ^{45}Sc nuclear magnetic resonance. Chem Mater 27:6660–6667

Pal B, Ariya PA (2004) Gas-phase HO•-initiated reactions of elemental mercury: kinetics, product studies, and atmospheric implications. Environ Sci Technol 38:5555–5566

Pacyna EG, Pacyna JM, Sundseth K, Munthe J, Kindbom K, Wilson S, Steenhuisen F, Maxson P (2010) Global emission of mercury to the atmosphere from anthropogenic sources in 2005 and projections to 2020. Atmos Environ 44:2487–2499

Pennington AM, Okonmah AI, Munoz DT, Tsilomelekis G, Celik FE (2018) Changes in polymorph composition in P25-TiO_2 during pretreatment analyzed by differential diffuse reflectance spectral analysis. J Phys Chem C 122:5093–5104

Pitoniak E, Wu CY, Londeree D, Mazyck D, Bonzongo JC, Powers K, Sigmund W (2003) Nanostructured silica-gel doped with TiO_2 for mercury vapor control. J Nanopart Res 5:281–292

Redmond G, Fitzmaurice D, Graetzel M (1993) Effect of surface chelation on the energy of an intraband surface state of a nanocrystalline titania film. J Phys Chem 97:6951–6954

Rivera-Reyna N, Hinojosa-Reyes L, Guzmán-Mar JL, Cai Y, O'Shea K, Hernández-Ramírez A (2013) Photocatalytical removal of inorganic and organic arsenic species from aqueous solution using zinc oxide semiconductor. Photochem Photobiol Sci 12:653–659

Saraf LV, Patil SI, Ogale SB, Sainkar SR, Kshirsager ST (1998) Synthesis of nanophase TiO_2 by ion beam sputtering and cold condensation technique. Int J Mod Phys B 12:2635–2647

San N, Hatipoğlu A, Koçtürk G, Çınar Z (2002) Photocatalytic degradation of 4-nitrophenol in aqueous TiO_2 suspensions: theoretical prediction of the intermediates. J Photochem Photobio A 146:189–197

Serpone N, Lawless D, Khairutdinov R (1995) Size effects on the photophysical properties of colloidal anatase TiO_2 particles: size quantization versus direct transitions in this indirect semiconductor? J Phys Chem 99:16646–16654

Shaban M, Abukhadra MR, Nasief FM, El-Salam HMA (2017) Removal of ammonia from aqueous solutions, ground water, and wastewater using mechanically activated clinoptilolite and synthetic zeolite-A: kinetic and equilibrium studies. Water Air Soil Pollut 228:450

Shaban M, Abukhadra MR, Rabia M, Elkader YA, El-Halim MRA (2018) Investigation the adsorption properties of graphene oxide and polyaniline nano/micro structures for efficient removal of toxic Cr(VI) contaminants from aqueous solutions; kinetic and equilibrium studies. Rend Lincei Sci Fis 29:141–154

Sharma VK, Sohn M (2009) Aquatic arsenic: toxicity, speciation, transformations, and remediation. Environ Int 35:743–759

Sing KS (1985) Reporting physisorption data for gas/solid systems with special reference to the determination of surface area and porosity. Pure Appl Chem 57:603–619

Tang H, Berger H, Schmid PE, Lévy F, Burri G (1993) Photoluminescence in TiO_2 anatase single crystals. Solid State Commun 87:847–850

Tang H, Berger H, Schmid PE, Lévy F (1994) Optical properties of anatase (TiO_2). Solid State Commun 92:267–271

Tian B, Zhang J (2012) Morphology-controlled synthesis and applications of silver halide photocatalytic materials. Catal Surv Jpn 16:210–230

Tian B, Dong R, Zhang J, Bao S, Yang F, Zhang J (2014) Sandwich-structured AgCl@Ag@TiO_2 with excellent visible-light photocatalytic activity for organic pollutant degradation and *E. coli* K12 inactivation. Appl Catal B 158:76–84

Tsai CY, Liu CW, Fan C, Hsi HC, Chang TY (2017) Synthesis of a SnO_2/TNT heterojunction nanocomposite as a high-performance photocatalyst. J Phys Chem C 121:6050–6059

Wang P, Huang B, Qin X, Zhang X, Dai Y, Wei J, Whangbo MH (2008) Ag@ AgCl: a highly efficient and stable photocatalyst active under visible light. Angew Chem Int Ed 47:7931–7933

Wang C, Shao C, Zhang X, Liu Y (2009) SnO_2 nanostructures-TiO_2 nanofibers heterostructures: controlled fabrication and high photocatalytic properties. Inorg Chem 48:7261–7268

Wang ZH, Jiang SD, Zhu YQ, Zhou JS, Zhou JH, Li ZS, Cen KF (2010) Investigation on elemental mercury oxidation mechanism by non-thermal plasma treatment. Fuel Process Technol 91:1395–1400

Wang H, Zhou S, Xiao L, Wang Y, Liu Y, Wu Z (2011) Titania nanotubes—a unique photocatalyst and adsorbent for elemental mercury removal. Catal Today 175:202–208

Wang XK, Wang C, Jiang WQ, Guo WL, Wang JG (2012) Sonochemical synthesis and characterization of Cl-doped TiO_2 and its application in the photodegradation of phthalate ester under visible light irradiation. Chem Eng J 189:288–294

Wendt S, Schaub R, Matthiesen J, Vestergaard EK, Wahlström E, Rasmussen MD, Thostrup P, Molina LM, Lægsgaard E, Stensgaard I, Hammer B, Besenbacher F (2005) Oxygen vacancies on TiO_2 (110) and their interaction with H_2O and O_2: a combined high-resolution STM and DFT study. Surf Sci 598:226–245

Wei ZG, Zou YD, Zeng HX, Zhong XC, Cheng ZJ, Xie SG (2011) Density functional theory calculations of arsenic(V) structures on perfect TiO_2 anatase (101) surface. Adv Mater Res 233-235:495–498

Wei Z, Liang K, Wu Y, Zou Y, Zuo J, Arriagada DC, Zhanchang P, Hu G (2016) The effect of pH on the adsorption of arsenic(III) and arsenic(V) at the TiO_2 anatase [1 0 1] surface. J Colloid Interface Sci 462:252–259

Wold A (1993) Photocatalytic properties of titanium dioxide (TiO_2). Chem Mater 5:280–283

Wu CY, Lee TG, Tyree G, Arar E, Biswas P (1998) Capture of mercury in combustion systems by in situ–generated titania particles with UV irradiation. Environ Eng Sci 15:137–148

Xiao Q, Si Z, Zhang J, Xiao C, Tan X (2008) Photoinduced hydroxyl radical and photocatalytic activity of samarium-doped TiO_2 nanocrystalline. J Hazard Mater 150:62–67

Xin B, Ding D, Gao Y, Jin X, Fu H, Wang P (2009) Preparation of nanocrystalline Sn–TiO_{2-X} via a rapid and simple stannous chemical reducing route. Appl Surf Sci 255:5896–5901

Yee MSL, Khiew PS, Lim SS, Chiu WS, Tan YF, Kok YY, Leong CO (2017) Enhanced marine antifouling performance of silver-titania nanotube composites from hydrothermal processing. Colloids Surf A Physicochem Eng Asp 520:701–711

Yu C, Jimmy CY (2009) A simple way to prepare C–N-codoped TiO_2 photocatalyst with visible-light activity. Catal Lett 129:462–470

Yu J, Dai G, Huang B (2009) Fabrication and characterization of visible-light-driven plasmonic photocatalyst Ag/AgCl/TiO_2 nanotube arrays. J Phys Chem C 113:16394–16401

Zhao Y, Hao R, Guo Q (2014) A novel pre-oxidation method for elemental mercury removal utilizing a complex vaporized absorbent. J Hazard Mater 280:118–126

Zhao Y, Hao R (2014) Macrokinetics of Hg^0 removal by a vaporized multicomponent oxidant. Ind Eng Chem Res 53:10899–10905

Zhao X, Zhang J, Wang B, Zada A, Humayun M (2015) Biochemical synthesis of Ag/AgCl nanoparticles for visible-light-driven photocatalytic removal of colored dyes. Materials 8:2043–2053